Environmental Science & Technology
pubs.acs.org/est
Article

Surface-Engineered Nanomaterials in Water: Understanding Critical Dynamics of Soft Organic Coatings and Relative Aggregation Density

Changwoo Kim and John D. Fortner*

Cite This: *Environ. Sci. Technol.* 2020, 54, 13548−13555
Read Online

ABSTRACT: Inorganic−organic nanocomposites, typically as an inorganic core with surface organic coating(s), have received interest as potential platform materials for sensor, catalyst, sorbent, and environmental applications, among others. Here, we describe the critical role of organic surface coatings with regard to the colloidal stability of engineered manganese oxide nanoparticles (Mn_xO_y NPs). Specifically, we prepared libraries of monodisperse Mn_xO_y NPs with a serial selection of surface coatings (stearic acid (SA), oleic acid (OA), poly(maleic anhydride-*alt*-1-octadecene) (PMAO), linear polyethyleneimine (LPEI), and multibranched polyethyleneimine (BPEI)), which were chosen based on comparable structure(s) and functional group(s). We systematically evaluated the role of surface organic coatings via critical coagulation concentrations (CCCs), which were compared with theoretical calculations (Schulze−Hardy rule). Through a newly developed light scattering protocol, we observed that the effective density of nanoclusters can exceed NPs' primary (bulk) density depending on the open space(s) within organic coatings. Interestingly, PMAO-coated NPs were more stable at the point of zero charge (PZC) than at neutral pH (pH 7), despite the loss of effective surface charge potential. CCC was 334 mM in NaCl and 1.5 mM in $CaCl_2$ at pH 7, compared to CCC values of 807 mM in NaCl and 210 mM in $CaCl_2$ at PZC. This increase in stability is due to polymer (re)configuration (at PZC), which was further confirmed with a quartz crystal microbalance-based technique to evaluate surface-based polymer dynamics. Taken together, this work quantifies the role of organic coating dynamics, including structure, grafting density, and configuration on the colloidal stability of organic-coated NPs.

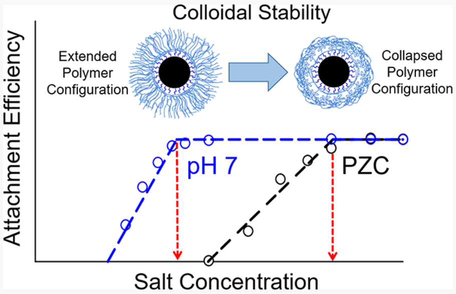

■ INTRODUCTION

In a solution, nanoscale particles aggregate when the free energy of the system is reduced by decreasing the total surface area.[1,2] Particle aggregation can strongly influence reactivity, including toxicity and persistence, in addition to playing a critical role in particle(s) fate and transport.[3−7] For charge-stabilized nanomaterials, the stability ratio (reciprocal value of attachment efficiency) provides fundamental insight into particle stability regimes.[8−10] Practically, this is measured by critical coagulation concentration (CCC), directly calculated via stability ratios, which are widely used as a practical index for evaluating and comparing the stability of nanomaterials in water.[11−13] According to the classical Derjaguin−Landau−Verwey−Overbeek (DLVO) theory, electrostatic double layer (EDL) repulsion is reduced as a function of counterion concentration and valence through the effective decrease of Debye screening length (surface charge screening).[14−16]

There are a number of approaches for evaluating the CCC (colloidal stability) of nanosized materials on the basis of classical DLVO interactions.[17−21] For most, CCC relationships are described in terms of the counter valence ion concentration as described by the Schulze−Hardy rule, which is derived from the linear superposition of Gouy−Chapman and unretarded Hamaker expressions (i.e., classical DLVO theory).[18,21] Such DLVO expressions, including the Schulze−Hardy rule, have theoretical limitations when asymmetric ions are incorporated as the Taylor series expansion of the Poisson−Boltzmann equation (involved in the description of EDL) can be simplified only when considering symmetric electrolytes.[22−24] Without such simplifications, complex numerical computational approaches are required. Despite this limitation, the Schulze−Hardy rule is widely accepted when describing monovalent and asymmetric divalent counterion dynamics.[25,26] Interestingly, when (nano)materials are coated or encapsulated by organic substances, such as artificial surfactants and organic matter, the Schulze−Hardy rule has been observed to be invalid.[25] As the Schulze−Hardy rule only considers classical DLVO interactions, extended DLVO (XDLVO) interactions

Received: April 7, 2020
Revised: August 9, 2020
Accepted: September 30, 2020
Published: October 15, 2020

have been explored to better describe the behavior of particles with organic coatings in water.

Organic surface coatings can provide EDL repulsion as well as XDLVO interactions, such as osmotic and elastic−steric repulsion, typically enhancing colloidal stability.[27−30] While a number of studies have explored XDLVO interactions for (soft) coated NPs,[31−34] outstanding questions remain regarding fundamental colloidal behavior as a function of organic coating(s) in terms of structure, grafting density, polymer dynamics, and solution chemistry. In particular, quantifying the role of organic coatings remains a challenge from a colloidal stability and (net) aggregation density perspective.

In this work, we explore the role of organic coatings on the stability of NPs with regard to the structure (bilayer, linear polymeric, and multibranched polymeric) and conformation dynamics (e.g., shrinking and/or stretching of polymer chains). We have designed and synthesized monodisperse manganese oxide (Mn_xO_y) core NPs with serially varied organic surface coatings (polymer- and organic acid-based) and an inorganic shell (silica), for comparison. As a function of solution chemistry, we quantify and compare the role of coating structure and polymer dynamics, as it relates to particle stability, through critical CCCs. Additionally, we present a novel method to determine the relative aggregation density and demonstrate that, under certain conditions, aggregates can actually have a higher density than the organic-coated particles (with extended coatings) themselves. Polymer configuration dynamics were further explored using a quartz crystal microbalance.

■ MATERIALS AND METHODS

Chemicals. Manganese(II) chloride tetrahydrate ($MnCl_2 \cdot 4H_2O$), oleic acid (OA), 1-octadecene (1-ODE), stearic acid (SA), poly(maleic anhydride-*alt*-1-octadecene) (PMAO), linear polyethyleneimine (LPEI), branched polyethyleneimine (BPEI, MW), Igepal CO-520, tetraethoxy orthosilicate (TEOS), poly-L-lysine hydrobromide (PLL), cyclohexane, ethanol, acetone, and hexane were purchased from Sigma-Aldrich. Sodium oleate was obtained from TCI America. Nanosilica was obtained from NanoComposix. Detail information is presented in the Supporting Information.

Synthesis of Manganese Oxide Nanoparticles and Functionalization. Mn_xO_y NPs were synthesized via manganese oleate (Mn-oleate) decomposition at 320 °C for 1 h under argon gas purging. Mn-oleate was synthesized by the method reported by An et al.[35] The mixtures of manganese chloride tetrahydrate (40 mmol) with OA (80 mmol) in ethanol (100 mL), water (50 mL), and hexane (80 mL) were heated at 58 °C for 4 h. The resulting Mn-oleate suspension was purified more than six times using water and ethanol (1:1 volume ratio) and then extracted the purified Mn-oleate using hexane. The size of M_xO_y NPs was controlled by Mn-oleate concentration; for 14, 18, and 25 nm M_xO_y NPs, 0.5, 1.0, and 2.0 mmol of the precursor were used in the presence of OA (0.5 mmol) in 1-ODE (5 g), respectively. The resulting NPs were purified using ethanol (20 mL) and acetone (25 mL). The purifying process was repeated more than six times. The purified Mn_xO_y NPs were stored in nonpolar solvent hexane. The resulting Mn_xO_y NPs were phase-transferred using OA, SA, PMAO, LPEI, and BPEI by ligand exchange[36] or encapsulation methods.[37] Chemical structure(s) of coating materials is presented in Table S1. Additional details regarding (organic) surface functionalization are also described in the Supporting Information.

Silica Coating. Silica coating on Mn_xO_y NPs was prepared based on the method reported by Selvan et al.[38,39] For details, Igepal CO-520 (2 mL) was added in cyclohexane (15 mL) containing 18 nm of synthesized Mn_xO_y NPs (40 mg). Then, 29% NH_4OH (0.4 mL) and TEOS (0.1 mL) were injected rapidly and the mixture was kept overnight with vigorous mixing. The resulting silica-coated NPs were purified more than six times using ethanol and DI using centrifugation.

Nanoparticle Characterization. The sizing of the synthesized Mn_xO_y NPs was accomplished using a transmission electron microscope (TEM, Tecnai G2 Spirit, FEI) with a carbon support film on 300 mesh copper grids (Electron Microscopy Sciences). The average NP size was determined by counting over a thousand of NPs using Image-Pro Plus 6.0 (Media Cybernetics).[40] X-ray diffraction (XRD) patterns (from 20 to 80° of 2θ) were measured using a powder diffractometer (Bruker d8 Advance X-ray Diffractometer) with Cu Kα radiation (1.54 Å). Phase-transferred NPs were characterized by dynamic light scattering (DLS, Malvern, Zetasizer Nano ZS, ZEN3600) to measure hydrodynamic diameters (D_H) and zeta potential (ζ). The number of surface-associated organic molecules, per cubic nm, was measured by total organic carbon (TOC, Shimadzu Scientific Instrument, TOC-L CPH/CPN).

Attachment Efficiency (α) and Critical Coagulation Concentration (CCC). Aggregation kinetics of NPs, as a function of NaCl and $CaCl_2$ concentration(s), was evaluated by measuring D_H of Mn_xO_y (1 ppm) at 22 °C. The pH was adjusted with NaOH or HNO_3 solution (0.01 M). Attachment efficiency (α) is calculated by the following equation

$$\alpha = \frac{1}{W} = \frac{k}{k_{fast}} \tag{1}$$

where W is the stability ratio, k is the reaction-limited aggregation rate constant, and k_{fast} is the diffusion-limited aggregation rate constant obtained under favorable aggregation conditions.[41−43] The CCC is the minimum salt concentration, whereby α becomes 1. Schulze−Hardy rule-based CCC estimates were calculated from a linear superposition Gouy−Chapman expression and unretarded Hamaker expression: $ccc \propto z^{-6}A^{-2}\tan h^{4}(ze\zeta/4kT)$, where z is valence, A is the Hamaker constant (J), e is the electron charge (1.602×10^{-19} C), ζ is the zeta potential (mV), k is the Boltzmann constant (1.380×10^{-23} J/K), and T (K) is the absolute temperature.[18,21]

Normalized Aggregate Density. The normalized aggregate density as a function of attachment efficiency was calculated by considering two types of number concentrations. One is the number concentration measured by DLS and another is the number concentration with aggregate spherical-shape assumption. Here, the number of nanoclusters was measured based upon DLS (intensity mean) using the photon count rate as an indicator of the number concentration via a Rayleigh scattering relationship.[44]

$$I = I_0\frac{\pi^4(1+\cos^2\theta)}{8R^2\lambda^4}\left(\frac{m^2-1}{m^2+2}\right)d^6N \tag{2}$$

where I is the scattered light intensity, I_0 is the incident light intensity, θ is the scattering angle, λ is the wavelength of the incident light, R is the distance of observation point and particles detected, m is the ratio of the refractive index of particles to the medium, d is the diameter of nanoparticles and/or nanoclusters, and N is the number concentration of NPs. eq 2 is reduced by applying a method coefficient term (β), which is constant regardless of experimental conditions.

$$I = I_0\beta\left(\frac{m^2 - 1}{m^2 + 2}\right)d^6N \tag{3}$$

The number of aggregates can be measured by knowing the information about the initial number concentration.[45,46]

$$\frac{P_t}{P_0} = \frac{d_t^{\,6}N_t}{d_0^{\,6}N_0} \tag{4}$$

where P is the derived photon count rate (kcps, count rate × attenuation index) and subscripts 0 and t indicate the initial and subsequent measurement times, respectively. The normalized aggregate density can then be obtained by dividing the two different number concentrations for two different times with spherical-shape assumption, typically starting with $t = 0$ (N_0/N_t). As shown in Figure S1, the number of NPs has a linear relationship with the photon count rate over a wide range of sizes from 23 to 208 nm (TEM measured) of silica NPs. Using silica NPs, we checked the validation of eq 4 by calculating P_0/d_0N_0 for each size of silica NPs (Figure S2). Data indicates that larger NPs (208 nm) can differ slightly, compared with smaller NPs (23−112 nm). It should be noted that there are other limitations to this approach as average aggregate diameters need to be below the wavelength of the incident light (632.8 nm, Rayleigh scattering criteria). Here, we measured clusters only under 200 nm; thus, we only evaluate and describe aggregate density for nanoclusters up to 200 nm using the last three measured points. For this, we also employed diluted initial NP concentration (1 ppm of NPs) to limit aggregates above 200 nm while having adequate photon count rate(s).

Quartz Crystal Microbalance with Dissipation (QCM-D). QCM-D (Q-sense E4, Biolin Scientific) with quartz sensor (5 MHz silica-coated QCM-D crystal, QSX-202, Q-sense) was used to evaluate the polymer dynamics at 22.00 ± 0.02 °C. PMAO coating was conducted by the "grafting to" method[47] using PLL as a linker.[16] PMAO saturated (stock) solution was prepared with 2 g/L of PMAO. Baseline experiments (with PLL-linked Q-sensor) were conducted for the compensation of undesired dissipation and the frequency shift caused by any difference in ionic strength (due to change in fluid viscosity). Fundamental to QCM-D, a measured frequency shift has a linear relationship with the deposited mass (Sauerbrey equation).[48]

$$m = -\frac{C\Delta F_n}{n} \tag{5}$$

Here, m is the total deposited mass on the Q-sensor, C is the quartz sensors constant, F_n is the shift in the resonance frequency, and n is the resonance number (n = 3). The dissipation shift provides insight into the viscoelastic properties of the adsorbed layer on the sensor. The dissipation during the oscillation of Q-sensor is described as[49,50]

$$D = -\frac{E_d}{2\pi E_s} \tag{6}$$

where D is the energy dissipation, E_d is the energy dissipated during one oscillation, and E_s is the energy stored in the oscillation system.

RESULTS AND DISCUSSION

Synthesis and Characterizations. By controlling the initial Mn-oleate concentration during synthesis, three sizes of monodisperse Mn_xO_y NPs were produced: 13.8 ± 1.4, 18.4 ± 1.5, and 24.6 ± 1.3 nm (Figures 1, S3, and S4). As shown in Figure S5a, X-ray diffraction (XRD) patterns matched MnO (JCPDS Card # 07-0230) and Mn_3O_4 (JCPDS Card # 24-0734), corresponding to the well-known MnO@Mn_3O_4 core−shell structure.[9,51]

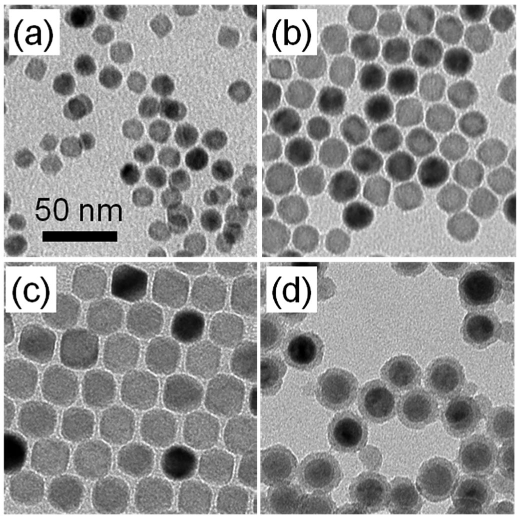

Figure 1. TEM images of monodisperse Mn_xO_y NPs (from (a) to (c)) and (d) silica encapsulated 18.4 nm Mn_xO_y NPs. Average diameter of NPs was measured by counting over 1000 NPs using Image-Pro 6.0: (a) 13.8 ± 1.4, (b) 18.4 ± 1.5, and (c) 24.6 ± 1.3 nm.

To achieve a serial library of particle coatings, synthesized Mn_xO_y NPs were surface-functionalized in a number of ways.[8,9] Mn_xO_y NPs with surface bilayer(s) were prepared by first surface stabilizing the particles in the organic phase upon formation, with OA (aligned with hydrophobic tail facing outwards). Particles were then phase-transferred via a second organic acid outer layer(s), such as OA and SA, with the functional head group facing outward, thus effectively rendering the particle surface hydrophilic. As shown in Figure S6a, an optimized bilayer structure (arrangement/concentration) was achieved by adjusting ligand(s) concentration(s). Poor dispersion and/or low stability resulted at above or below the optimal organic acid concentrations. For example, 35.4 μmol of OA was the optimized concentration for phase transfer of a particular concentration (0.16 g/L or 1.8×10^{17} particles/L) of Mn_xO_y NPs. Above critical micelle concentrations (CMC), organic acids (OA and SA) form micelles in the water phase, leading to the removal of the surfactant from the surface of NPs and decreasing the NP stability.[37] Below optimal concentrations, colloidal stability decreases due to insufficient surface coating(s).

Polymer-stabilized Mn_xO_y NPs were prepared using negatively charged PMAO, positively charged linear polyethylenimine (LPEI), and multibranched PEI (BPEI). As presented in Figure S6b, above certain polymer concentrations, particle transfer is optimized; 0.32 μmol of BPEI was the

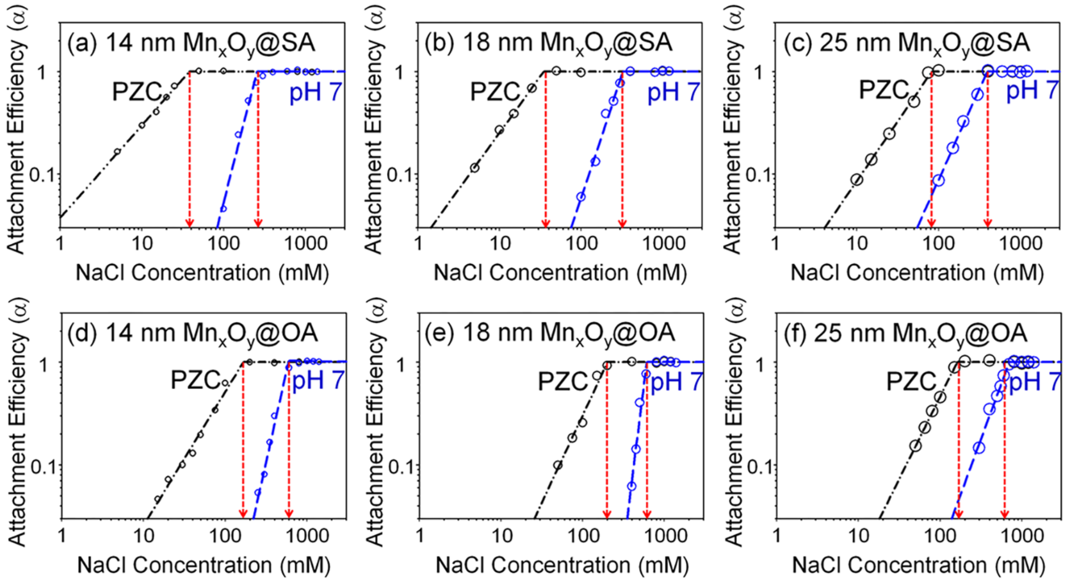

Figure 2. Attachment efficiency of bilayer-structured Mn_xO_y NPs as a function of NaCl concentration at pH 7.0 (blue) and at pH 4.0 (PZC, black); (a) 14 nm Mn_xO_y@SA, (b) 18 nm Mn_xO_y@SA, (c) 25 nm Mn_xO_y@SA, (d) 14 nm Mn_xO_y@OA, (e) 18 nm Mn_xO_y@OA, and (f) 25 nm Mn_xO_y@OA.

minimum concentration needed for optimal surface-stabilized Mn_xO_y NPs (0.16 g/L or 1.8 × 10^{17} particles/L). As a control (no organic coating), silica-coated 18 nm Mn_xO_y NPs were synthesized via a sol−gel method using TEOS as a silica source.[38,39] For these, silica shell thickness was controlled by the TEOS concentration,[38,39] resulting in a shell of approximately 3 nm. Hydrodynamic diameters (D_H), zeta potential (ζ), and number of surface-associated organic molecules (per cubic nm) of phase-transferred NPs are described in the Supporting Information (Figure S5).

Role of Bilayer Organic Structure on Colloidal Stability. Bilayer-structured coatings were evaluated for the three different-sized particles (14, 18, and 25 nm) with OA and SA outer coatings. Both SA and OA have 18 carbon chains with identical functional head groups (carboxyl). While SA is made of (sp^3) C18 linear carbon chain, OA is an unsaturated *cis*-C18 organic acid with a double bond between C9 and C10.[8] As shown in Figure 2, CCC values for both Mn_xO_y@SA and Mn_xO_y@OA were measured using NaCl at pH 7.0 ± 0.1. CCC values for 14, 18, and 25 nm Mn_xO_y NPs were 256, 326, and 392 mM for Mn_xO_y@SA, respectively, and 596, 609, and 702 mM for Mn_xO_y@OA, respectively. Here, larger NPs are actually more stable than smaller NPs. This is likely due to the fact that larger particles have significantly higher grafting density, which is presented here as the carbon (mass) density per surface area (grafting density ratio of 25 to 14 nm is 2.7 and 2.0 for SA and OA, respectively, as presented in Table S2).

Interestingly, for all NP sizes, Mn_xO_y@OA shows higher colloidal stability compared to Mn_xO_y@SA. To explore this further, CCC values for both Mn_xO_y@OA and Mn_xO_y@SA were additionally measured at a pH near the point of zero charge (PZC) to minimize the electrostatic double layer (EDL) repulsion. As pH was lowered, ζ of Mn_xO_y@SA and Mn_xO_y@OA decreased via protonation of the carboxyl group (Figure S7). At PZC (pH 3.5), Mn_xO_y@SA and Mn_xO_y@OA readily aggregated. We selected the pH of the solution at pH 4 (near the PZC) to prevent unwanted aggregation. At pH 4, ζ for 14, 18, and 25 nm Mn_xO_y@SA was −5.0, −4.2, and −4.5 mV, respectively, and ζ for 14, 18, and 25 nm Mn_xO_y@OA was −6.5, −5.5, and −4.7 mV, respectively. CCC values at pH 4 were 38, 35, and 83 mM for Mn_xO_y@SA, respectively, and 167, 202, and 162 mM for Mn_xO_y@OA, in the order of increasing size (Figure 2). For these, the main difference is that Mn_xO_y@OA contains a *cis* double bond in the second, out layer (OA, C8−C9 bond), compared to Mn_xO_y@SA, which does not (SA is saturated). In previous reports, our group observed that the restricted vibration and rotation of unsaturated carbon chains (OA) compared to saturated carbon chains (SA) leads to higher elastic−steric repulsive energies, which is likely due to lower net entropy-related effects.[8]

Surface Coating-Dependent Colloidal Stability. The effects of surface coating types on colloidal stability were evaluated using 18 nm M_xO_y NPs with three types of surface coatings: silica (M_xO_y@SiO_2), two bilayers (M_xO_y@SA and M_xO_y@OA), and a polymer (PMAO, MW = 40 K) (M_xO_y@PMAO). We chose M_xO_y@SiO_2 as a control due to insignificant osmotic or elastic−steric repulsion force considerations. As shown in Figure 3, the CCC values were measured using NaCl or $CaCl_2$ at pH 7.0 ± 0.1. All measured CCC values are presented in Table S3. CCC values in NaCl were 415 mM for M_xO_y@SiO_2, 609 mM for M_xO_y@OA, 326 mM for M_xO_y@SA, and 334 mM for M_xO_y@PMAO. Without (organic) surface stabilization, relatively high CCC values were observed for M_xO_y@SiO_2. We hypothesize that a silica coating effectively decreases vdW interactions; Hamaker constant (A_{121}) for silica (SiO_2) has been reported over a range from 0.63 × 10^{-20} to 0.85 × 10^{-20} J,[52−54] which is significantly lower than the Hamaker constant (A_{121}) for manganese oxides (7.84 × 10^{-20} J).[55] Interestingly, polymer-coated M_xO_y@PMAO has a smaller CCC (334 mM) than the bilayered M_xO_y@OA (609 mM). Grafting density also plays an important role with regard to steric repulsion.[27] Despite the fact that the surface loading (mass) for M_xO_y@PMAO was higher than M_xO_y@OA, the effective grafting density of M_xO_y@OA was 1.7 times higher than that of M_xO_y@PMAO (Table S2).

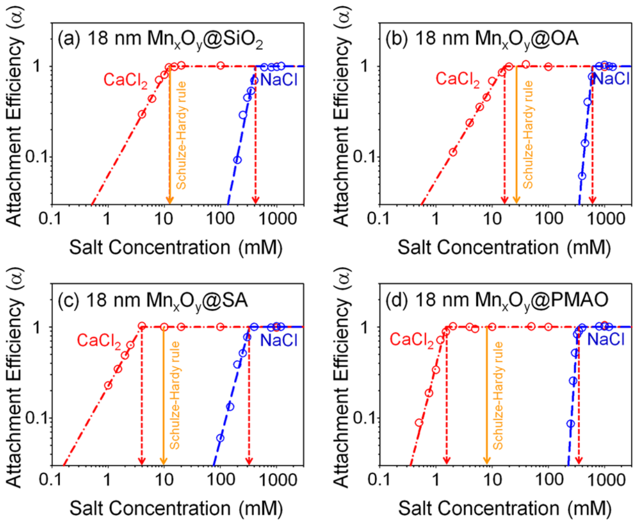

Figure 3. Attachment efficiency of surface-functionalized 18 nm Mn$_x$O$_y$ NPs ((a) Mn$_x$O$_y$@SiO$_2$, (b) Mn$_x$O$_y$@OA, (c) Mn$_x$O$_y$@SA, and (d) Mn$_x$O$_y$@PMAO) as a function of salt concentration (NaCl (blue) and CaCl$_2$ (red)) and Schulze−Hardy rule expectation (yellow line). Every CCC value was measured at pH 7.0 ± 0.1.

The Schulze−Hardy rule relates the valence of counterion(s) to colloidal stability via the classical DLVO approach (XDLVO interactions are not considered). To explore the effects of XDLVO interactions on colloidal stability, we compared experimentally measured CCC values in CaCl$_2$ and CCC calculated (modeled) by the Schulze−Hardy rule ($ccc \propto z^{-6}A^{-2}\tanh^4(ze\zeta/4kT)$).[17,20] As shown in Figure 3, CCC values in CaCl$_2$ for M$_x$O$_y$@SiO$_2$, M$_x$O$_y$@OA, M$_x$O$_y$@SA, and M$_x$O$_y$@PMAO were 12.0, 16.3, 3.8, and 1.5 mM (experimentally measured), respectively, and 12.6, 24.6, 9.9, and 7.9 mM (Schulze−Hardy rule), respectively. While M$_x$O$_y$@SiO$_2$ corresponds well with Schulze−Hardy expectations, organic-coated NPs deviated from Schulze−Hardy calculations. The percentage differences between them for M$_x$O$_y$@SiO$_2$, M$_x$O$_y$@OA, M$_x$O$_y$@SA, and M$_x$O$_y$@PMAO were 4, 50, 155, and 430%, respectively. Polymer-stabilized M$_x$O$_y$@PMAO has the largest difference between experimental measurements and Schulze−Hardy calculations. These differences are likely to be not only from XDLVO interactions but also (PMAO) configuration changes, which were further explored by QCM-D. Figure S8 presents the frequency and dissipation shift of the PMAO-grafted sensor as a function of salt concentration (NaCl or CaCl$_2$). With increasing NaCl concentration (up to 2 M NaCl), frequency shift decreases and the corresponding dissipation shift increases. This indicates that counterions (in this case as Na$^+$) can cause swelling-type interactions with PMAO.[49,56] For M$_x$O$_y$@PMAO particle systems, as the ionic strength is increased, the organic coating effectively decreases in density (i.e., expanding) and thus additional coating overlapping with other particles can occur. In contrast to monovalent counterions (Na$^+$), PMAO dynamics behave differently in the presence of divalent counterion (Ca^{2+}). From 1 to 20 mM CaCl$_2$, frequency shift decreases with a slightly increasing dissipation shift, indicative of PMAO swelling.[49,56] Higher CaCl$_2$ concentrations (20 mM−1 M) lead to the effective collapse of the PMAO, also releasing water molecules (adsorbed in PMAO) due to effective neutralization (screening) of functional groups (maleic anhydride)[49,57] Further, above 1 M (CaCl$_2$), the frequency again decreased (increasing dissipation), indicating re-expansion (rehydration) of the PMAO. Regarding the re-expansion at high ionic strength, we hypothesize that adsorbed Ca^{2+} ions are likely to form sufficient counterion complexes with oppositely charged (PMAO) functional groups, similar to particle restabilization via excess coagulant in water treatment.[58]

Effects of Polymer Structure and Configuration Change on Colloidal Stability. To elucidate the effects of polymer structure on particle stability, two differently structured PEI polymers (linear polyethylenimine (LPEI) and multibranched PEI (BPEI)) with identical MW and composition were employed. Figure 4a presents the attachment efficiency of M$_x$O$_y$@LPEI under varied ionic salt conditions at pH 7.0 ± 0.1. CCC values for these were 256 mM in NaCl and 139 mM in CaCl$_2$. For positively charged NPs, divalent cations (Ca^{2+}) do not significantly influence their stability and considering a classic DLVO model, CCC in NaCl should be 2 times higher than CCC in CaCl$_2$ (experimentally measured to be 1.8 times here). In contrast, M$_x$O$_y$@BPEI is extremely stable under 1 M (diffusion-limited regime of M$_x$O$_y$@LPEI) of NaCl or CaCl$_2$ concentration (Figure 4b). Multibranch polymers, here as BPEI, significantly hinder molecular overlap (interpenetration) as polymer segments are anchored throughout the polymer volume itself. This observation further highlights the importance of organic coating structure as it relates to colloidal stability.

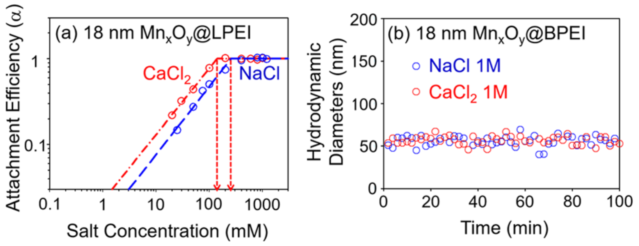

Figure 4. (a) Attachment efficiency of 18 nm Mn$_x$O$_y$@LPEI as a function of salt concentration (NaCl (blue) and CaCl$_2$ (red)) and (b) time-dependent hydrodynamic diameters of multibranched 18 nm Mn$_x$O$_y$@BPEI. All measurements were conducted at pH 7.0 ± 0.1.

Polymer configuration change can also play an important role in colloidal stability, yet polymer-coated NPs (M$_x$O$_y$@LPEI, M$_x$O$_y$@BPEI, and M$_x$O$_y$@PMAO) maintain similar (initial) hydrodynamic diameters at a PZC (Figure S9). To further explore this, CCC for M$_x$O$_y$@PMAO was measured for two different pH values (pH 7 and pH 2.5 (PZC)) considering both NaCl and CaCl$_2$. As shown in Figure 5a,b, CCC for M$_x$O$_y$@PMAO dramatically increased near the PZC, although NPs lost their effective surface charge (334 mM in NaCl and 1.5 mM in CaCl$_2$ at pH 7 vs 807 mM in NaCl and 210 mM in CaCl$_2$ at PZC). To better understand conformation changes, PMAO behavior was monitored at pH 7 and PZC using QCM-D. Figure 5c−e presents the frequency and dissipation (n = 3, 5, and 7) of a PMAO-coated sensor at pH 7 and PZC, oscillating the pH every 20 min for six cycles. As pH increased from PZC to 7.0, the frequency decreased (increasing dissipation) and then increased (decreasing dissipation) with decreasing pH from 7.0 to PZC. In other words, PMAO collapses (shrinking) at pH near PZC due to the release of sorbed water molecules and a charge neutralization while expanding at pH 7.[49,59] Based on these observations, it is likely

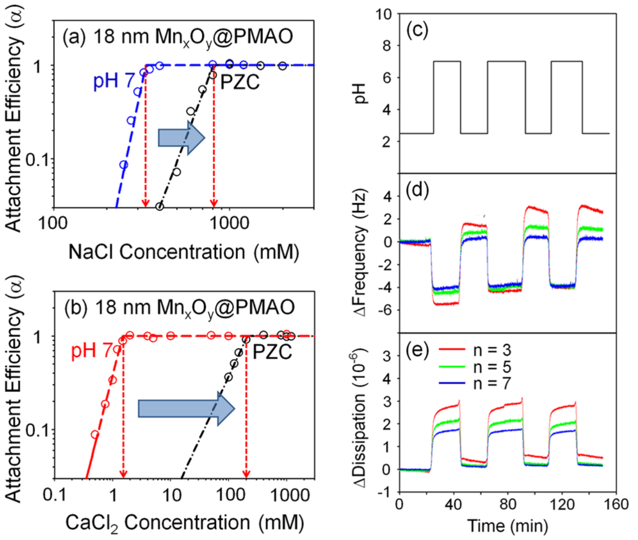

Figure 5. Attachment efficiency of 18 nm Mn$_x$O$_y$@PMAO as a function of (a) NaCl concentration and (b) CaCl$_2$ concentration at pH 7.0 and PZC. Frequency and dissipation shift of PMAO at pH 2.5 (PZC) and pH 7.0 with the overtone n = 3 (red), 5 (green), and 7 (blue); time-dependent (c) pH, (d) frequency, and (e) dissipation.

that the shrinkage/collapse dynamics of surface polymer chains significantly increase the colloidal stability of similar polymer-coated NPs by increasing elastic−steric repulsion due to a relatively more dense coating and hindering polymer interpenetration (overlap).

Surface Coating-Dependent Aggregation Density. As particles aggregate, the resulting aggregation (cluster) density is crucial to understand and predict effective surface area interactions and transport behavior.[60] To date, the effective aggregate density, as a function of organic surface coating(s), is not easily quantified in situ and in real time. Further, the aggregation behavior of organic-coated NPs is different from NP aggregation without surfactant or NOM due to the additional XDLVO interactions. When two NPs approach each other (collision), organic coating regime(s) can compress (increase the coating density), enhancing repulsion.[61] Further, upon aggregation, the overlap of the organic coating regime(s) is likely for some organic-coated NPs. For CCC experiments described (Figure 3), the normalized density, as a function of attachment efficiency, is quantified here by considering two types of number concentrations (the measured number concentration by DLS and the theoretical number concentration with spherical-shape assumption), as described in the Materials and Methods section.

Figure 6 shows the relative aggregate density as a function of attachment efficiency (varied through ionic strength, as NaCl). For these systems, the relative aggregate density (compared to the particle density itself, which includes coatings) is highly dependent on the coating structure(s). M$_x$O$_y$@SiO$_2$ aggregates have <0.6 normalized densities at low attachment efficiencies (α < 0.2), as shown in Figure 6a. In contrast, normalized densities of bilayer-coated NP aggregates (M$_x$O$_y$@SA and M$_x$O$_y$@OA) maintain their primary density under low attachment efficiency conditions (α < 0.1) (Figure 6b,c). Perhaps even more interesting, M$_x$O$_y$@PMAO has relative densities above 1 over a wide range of attachment efficiency conditions due to the overlap of M$_x$O$_y$@PMAO surface coating (Table S2). In addition, with increasing attachment efficiencies, the normalized density decreases regardless of the surface coating types. Under low attachment efficiency conditions (low ionic strength), NPs have a chance to penetrate into nanoclusters at effectively slower aggregation formation rates, leading to more dense aggregates. Under higher salt concentrations, with high(er) attachment coefficients, NPs attach (irreversibly) faster, resulting in lower relative aggregate densities.[18,62]

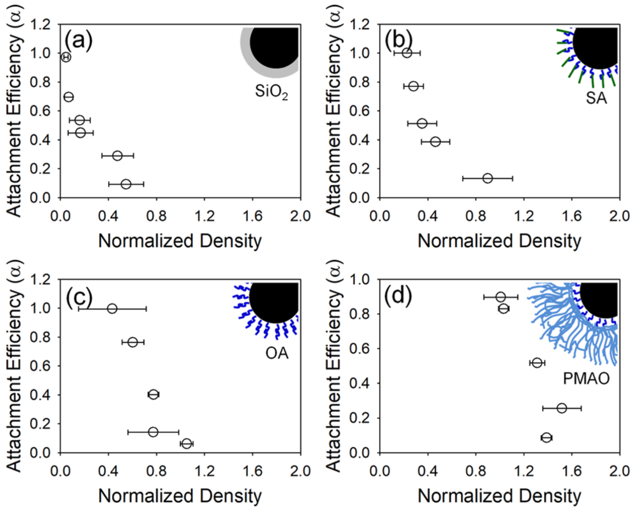

Figure 6. Normalized density of surface-coated 18 nm Mn$_x$O$_y$ NPs ((a) Mn$_x$O$_y$@SiO$_2$, (b) Mn$_x$O$_y$@SA, (c) Mn$_x$O$_y$@OA, and (d) Mn$_x$O$_y$@PMAO) as a function of attachment efficiency. Attachment efficiency was controlled using NaCl (at pH 7.0 ± 0.1).

To summarize, we systematically describe the critical role of organic surface coatings with respect to colloidal stability for serially varied nanoparticle library. For organic bilayer-coated NPs, the presence of a single double bond can significantly increase colloidal stability. Considering polymer-grafted NPs, we demonstrate that the polymer structure and dynamics play critical roles in NP stability. Through a newly developed DLS protocol, we demonstrate that the effective density of nanoparticle clusters can be measured in situ and in real time. Through this method, we observe that the relative aggregation density is highly dependent on the attachment efficiency and can even exceed a material's primary density by overlapping organic coatings (via interpenetration), as seen for open, dendritic polymer coatings. Taken together, this work highlights the complex nature of organic surface coatings as they govern nanoparticle behavior in water. Looking forward, studies considering nanoparticles with organic coatings should recognize such complexities by carefully characterizing coating structures, grafting densities, and potential configuration changes, as they relate to both particle and aggregate properties and aqueous behavior(s).

■ ASSOCIATED CONTENT

Supporting Information

The Supporting Information is available free of charge at https://pubs.acs.org/doi/10.1021/acs.est.0c02137.

The histograms of NPs; diameters of NPs as a function of Mn-oleate concentration; characterization of NPs; hydrodynamic diameters of NPs as a function of surfactant concentration; van der Waals energy interaction of NPs; frequency and dissipation shift; and photon counter rate as a function of the number of NPs (PDF)

■ AUTHOR INFORMATION

Corresponding Author

John D. Fortner − *Department of Chemical and Environmental Engineering, Yale University, New Haven, Connecticut 06520, United States;* orcid.org/0000-0002-3669-779X; Phone: +1-314-935-9293; Email: john.fortner@yale.edu

Author

Changwoo Kim − *Department of Chemical and Environmental Engineering, Yale University, New Haven, Connecticut 06520, United States;* orcid.org/0000-0002-8117-842X

Complete contact information is available at: https://pubs.acs.org/10.1021/acs.est.0c02137

Notes

The authors declare no competing financial interest.

■ ACKNOWLEDGMENTS

This work is supported by U.S. Army Corps of Engineers (W912HZ-13-2-0009-P00001), the U.S. Department of Agriculture, NIFA (2018-67021-28319), and the U.S. National Science Foundation (CBET 1437820 and CBET 1704326). XRD measurements were made possible by a grant from the U.S. National Science Foundation (EAR-1161543). TEM, DLS, and ICP-OES were provided by the Nano Research Facility (NRF) at Washington University in St. Louis, a member of the National Nanotechnology Infrastructure Network (NNIN), which is supported by the National Science Foundation (ECS-0335765).

■ REFERENCES

(1) Spagnoli, D.; Banfield, J. F.; Parker, S. C. Free energy change of aggregation of nanoparticles. *J. Phys. Chem. C* **2008**, *112*, 14731−14736.

(2) Auffan, M.; Rose, J.; Bottero, J.-Y.; Lowry, G. V.; Jolivet, J.-P.; Wiesner, M. R. Towards a definition of inorganic nanoparticles from an environmental, health and safety perspective. *Nat. Nanotechnol.* **2009**, *4*, 634−641.

(3) Kim, C.; Lee, S. Effect of seepage velocity on the attachment efficiency of TiO_2 nanoparticles in porous media. *J. Hazard. Mater.* **2014**, *279*, 163−168.

(4) Liu, J.; Lu, Y. Stimuli-responsive disassembly of nanoparticle aggregates for light-up colorimetric sensing. *J. Am. Chem. Soc.* **2005**, *127*, 12677−12683.

(5) Li, X.; Lenhart, J. J.; Walker, H. W. Dissolution-accompanied aggregation kinetics of silver nanoparticles. *Langmuir* **2010**, *26*, 16690−16698.

(6) Sharma, V. K. Aggregation and toxicity of titanium dioxide nanoparticles in aquatic environment—a review. *J. Environ. Sci. Health, Part A* **2009**, *44*, 1485−1495.

(7) Aruoja, V.; Dubourguier, H.-C.; Kasemets, K.; Kahru, A. Toxicity of nanoparticles of CuO, ZnO and TiO_2 to microalgae Pseudokirchneriella subcapitata. *Sci. Total Environ.* **2009**, *407*, 1461−1468.

(8) Lee, S. S.; Li, W.; Kim, C.; Cho, M.; Lafferty, B. J.; Fortner, J. D. Surface functionalized manganese ferrite nanocrystals for enhanced uranium sorption and separation in water. *J. Mater. Chem. A* **2015**, *3*, 21930−21939.

(9) Lee, S. S.; Li, W.; Kim, C.; Cho, M.; Catalano, J. G.; Lafferty, B. J.; Decuzzi, P.; Fortner, J. D. Engineered manganese oxide nanocrystals for enhanced uranyl sorption and separation. *Environ. Sci.: Nano* **2015**, *2*, 500−508.

(10) Li, W.; Liu, D.; Wu, J.; Kim, C.; Fortner, J. D. Aqueous Aggregation and Surface Deposition Processes of Engineered Superparamagnetic Iron Oxide Nanoparticles for Environmental Applications. *Environ. Sci. Technol.* **2014**, *48*, 11892−11900.

(11) Gallego-Urrea, J. A.; Holmberg, J. P.; Hassellöv, M. Influence of different types of natural organic matter on titania nanoparticle stability: effects of counter ion concentration and pH. *Environ. Sci.: Nano* **2014**, *1*, 181−189.

(12) Huynh, K. A.; Chen, K. L. Aggregation kinetics of citrate and polyvinylpyrrolidone coated silver nanoparticles in monovalent and divalent electrolyte solutions. *Environ. Sci. Technol.* **2011**, *45*, 5564−5571.

(13) Hu, J.-D.; Zevi, Y.; Kou, X.-M.; Xiao, J.; Wang, X.-J.; Jin, Y. Effect of dissolved organic matter on the stability of magnetite nanoparticles under different pH and ionic strength conditions. *Sci. Total Environ.* **2010**, *408*, 3477−3489.

(14) Tagliaro, I.; Di Credico, B.; Moncho-Jordá, A. Electrostatic depletion effects on the stability of colloidal dispersions of sepiolite and natural rubber latex. *J. Colloid Interface Sci.* **2020**, *560*, 606−617.

(15) Wang, Y.; Yang, K.; Chefetz, B.; Xing, B.; Lin, D. The pH and concentration dependent interfacial interaction and heteroaggregation between nanoparticulate zero-valent iron and clay mineral particles. *Environ. Sci.: Nano* **2019**, *6*, 2129−2140.

(16) Town, R. M.; Duval, J. F.; van Leeuwen, H. P. The intrinsic stability of metal ion complexes with nanoparticulate fulvic acids. *Environ. Sci. Technol.* **2018**, *52*, 11682−11690.

(17) Reerink, H.; Overbeek, J. T. G. The rate of coagulation as a measure of the stability of silver iodide sols. *Discuss. Faraday Soc.* **1954**, *18*, 74−84.

(18) Elimelech, M.; Gregory, J.; Jia, X. *Particle Deposition and Aggregation: Measurement, Modelling and Simulation*; Butterworth-Heinemann, 2013.

(19) Fuchs, N. Über die stabilität und aufladung der aerosole. *Z. Phys.* **1934**, *89*, 736−743.

(20) Chen, K. L.; Elimelech, M. Influence of humic acid on the aggregation kinetics of fullerene (C 60) nanoparticles in monovalent and divalent electrolyte solutions. *J. Colloid Interface Sci.* **2007**, *309*, 126−134.

(21) Chen, K. L.; Elimelech, M. Aggregation and deposition kinetics of fullerene (C60) nanoparticles. *Langmuir* **2006**, *22*, 10994−11001.

(22) Moroi, Y. Stability of Colloidal Particles. In *Micelles*; Springer, 1992; pp 131−148.

(23) de Carvalho, S. J.; Fenley, M. O.; da Silva, F. L. sB. Protein−Ion Binding Process on Finite Macromolecular Concentration. A Poisson−Boltzmann and Monte Carlo Study. *J. Phys. Chem. B* **2008**, *112*, 16766−16776.

(24) Das, P. K.; Bhattacharjee, S.; Moussa, W. Electrostatic double layer force between two spherical particles in a straight cylindrical capillary: finite element analysis. *Langmuir* **2003**, *19*, 4162−4172.

(25) Lin, D.; Ma, S.; Zhou, K.; Wu, F.; Yang, K. The effect of water chemistry on homoaggregations of various nanoparticles: Specific role of Cl− ions. *J. Colloid Interface Sci.* **2015**, *450*, 272−278.

(26) Shih, Y.-h.; Zhuang, C.-m.; Tso, C.-p.; Lin, C.-h. The effect of electrolytes on the aggregation kinetics of titanium dioxide nanoparticle aggregates. *J. Nanopart. Res.* **2012**, *14*, No. 924.

(27) Hotze, E. M.; Phenrat, T.; Lowry, G. V. Nanoparticle aggregation: challenges to understanding transport and reactivity in the environment. *J. Environ. Qual.* **2010**, *39*, 1909−1924.

(28) Phenrat, T.; Saleh, N.; Sirk, K.; Kim, H.-J.; Tilton, R. D.; Lowry, G. V. Stabilization of aqueous nanoscale zerovalent iron dispersions by anionic polyelectrolytes: adsorbed anionic polyelectrolyte layer properties and their effect on aggregation and sedimentation. *J. Nanopart. Res.* **2008**, *10*, 795−814.

(29) Ortega-Vinuesa, J.; Martın-Rodrıguez, A.; Hidalgo-Alvarez, R. Colloidal stability of polymer colloids with different interfacial properties: mechanisms. *J. Colloid Interface Sci.* **1996**, *184*, 259−267.

(30) Fritz, G.; Schädler, V.; Willenbacher, N.; Wagner, N. J. Electrosteric stabilization of colloidal dispersions. *Langmuir* **2002**, *18*, 6381−6390.

(31) Lodeiro, P.; Achterberg, E. P.; Rey-Castro, C.; El-Shahawi, M. S. Effect of polymer coating composition on the aggregation rates of Ag nanoparticles in NaCl solutions and seawaters. *Sci. Total Environ.* **2018**, *631*−*632*, 1153−1162.

(32) You, G.; Hou, J.; Wang, P.; Xu, Y.; Wang, C.; Miao, L.; Lv, B.; Yang, Y.; Luo, H. Effects of CeO2 nanoparticles on sludge aggregation and the role of extracellular polymeric substances−explanation based on extended DLVO. *Environ. Res.* **2016**, *151*, 698−705.

(33) Li, Z.; Shakiba, S.; Deng, N.; Chen, J.; Louie, S. M.; Hu, Y. Natural Organic Matter (NOM) Imparts Molecular-Weight-Dependent Steric Stabilization or Electrostatic Destabilization to Ferrihydrite Nanoparticles. *Environ. Sci. Technol.* **2020**, *54*, 6761−6770.

(34) Nakahashi, Y.; Unoura, K.; Nabika, H. Non-DLVO Aggregation of Gold Nanoparticles Modified with Amino Acids. *Chem. Lett.* **2016**, *45*, 946−948.

(35) An, K.; Park, M.; Yu, J. H.; Na, H. B.; Lee, N.; Park, J.; Choi, S. H.; Song, I. C.; Moon, W. K.; Hyeon, T. Synthesis of Uniformly Sized Manganese Oxide Nanocrystals with Various Sizes and Shapes and Characterization of Their T1 Magnetic Resonance Relaxivity. *Eur. J. Inorg. Chem.* **2012**, 2148−2155.

(36) Sperling, R. A.; Parak, W. J. Surface modification, functionalization and bioconjugation of colloidal inorganic nanoparticles. *Philos. Trans. R. Soc., A* **2010**, *2012*, 1333−1383.

(37) Prakash, A.; Zhu, H.; Jones, C. J.; Benoit, D. N.; Ellsworth, A. Z.; Bryant, E. L.; Colvin, V. L. Bilayers as phase transfer agents for nanocrystals prepared in nonpolar solvents. *ACS Nano* **2009**, *3*, 2139−2146.

(38) Selvan, S.; Patra, P. K.; Ang, C. Y.; Ying, J. Y. Synthesis of silica-coated semiconductor and magnetic quantum dots and their use in the imaging of live cells. *Angew. Chem., Int. Ed.* **2007**, *46*, 2448−2452.

(39) Selvan, S. T.; Tan, T. T.; Ying, J. Y. Robust, Non-Cytotoxic, Silica-Coated CdSe Quantum Dots with Efficient Photoluminescence. *Adv. Mater.* **2005**, *17*, 1620−1625.

(40) Vigneau, E.; Loisel, C.; Devaux, M.; Cantoni, P. Number of particles for the determination of size distribution from microscopic images. *Powder Technol.* **2000**, *107*, 243−250.

(41) Mylon, S. E.; Chen, K. L.; Elimelech, M. Influence of natural organic matter and ionic composition on the kinetics and structure of hematite colloid aggregation: Implications to iron depletion in estuaries. *Langmuir* **2004**, *20*, 9000−9006.

(42) Holthoff, H.; Egelhaaf, S. U.; Borkovec, M.; Schurtenberger, P.; Sticher, H. Coagulation rate measurements of colloidal particles by simultaneous static and dynamic light scattering. *Langmuir* **1996**, *12*, 5541−5549.

(43) Chen, K. L.; Mylon, S. E.; Elimelech, M. Aggregation kinetics of alginate-coated hematite nanoparticles in monovalent and divalent electrolytes. *Environ. Sci. Technol.* **2006**, *40*, 1516−1523.

(44) Vysotskii, V.; Uryupina, O. Y.; Gusel'nikova, A.; Roldugin, V. On the feasibility of determining nanoparticle concentration by the dynamic light scattering method. *Colloid J.* **2009**, *71*, 739−744.

(45) Shang, J.; Gao, X. Nanoparticle counting: towards accurate determination of the molar concentration. *Chem. Soc. Rev.* **2014**, *43*, 7267−7278.

(46) Liu, X.; Dai, Q.; Austin, L.; Coutts, J.; Knowles, G.; Zou, J.; Chen, H.; Huo, Q. A one-step homogeneous immunoassay for cancer biomarker detection using gold nanoparticle probes coupled with dynamic light scattering. *J. Am. Chem. Soc.* **2008**, *130*, 2780−2782.

(47) Minko, S. Grafting on Solid Surfaces:"Grafting to" and "Grafting from" Methods. In *Polymer Surfaces and Interfaces*; Springer, 2008; pp 215−234.

(48) Dixon, M. C. Quartz crystal microbalance with dissipation monitoring: enabling real-time characterization of biological materials and their interactions. *J. Biomol. Tech.* **2008**, *19*, 151−158.

(49) Liu, G.; Zhang, G. *QCM-D Studies on Polymer Behavior at Interfaces*; Springer, 2013.

(50) Rodahl, M.; Höök, F.; Krozer, A.; Brzezinski, P.; Kasemo, B. Quartz crystal microbalance setup for frequency and Q-factor measurements in gaseous and liquid environments. *Rev. Sci. Instrum.* **1995**, *66*, 3924−3930.

(51) An, K.; Park, M.; Yu, J. H.; Na, H. B.; Lee, N.; Park, J.; Choi, S. H.; Song, I. C.; Moon, W. K.; Hyeon, T. Synthesis of uniformly sized manganese oxide nanocrystals with various sizes and shapes and characterization of their T1 magnetic resonance relaxivity. *Eur. J. Inorg. Chem.* **2012**, *2012*, 2148−2155.

(52) Israelachvili, J. N. *Intermolecular and Surface Forces: Revised Third Edition*; Academic Press, 2011.

(53) Butt, H.-J.; Cappella, B.; Kappl, M. Force measurements with the atomic force microscope: Technique, interpretation and applications. *Surf. Sci. Rep.* **2005**, *59*, 1−152.

(54) Petosa, A. R.; Jaisi, D. P.; Quevedo, I. R.; Elimelech, M.; Tufenkji, N. Aggregation and deposition of engineered nanomaterials in aquatic environments: role of physicochemical interactions. *Environ. Sci. Technol.* **2010**, *44*, 6532−6549.

(55) Huangfu, X.; Jiang, J.; Ma, J.; Liu, Y.; Yang, J. Aggregation kinetics of manganese dioxide colloids in aqueous solution: influence of humic substances and biomacromolecules. *Environ. Sci. Technol.* **2013**, *47*, 10285−10292.

(56) Dobrynin, A. V. Electrostatic persistence length of semiflexible and flexible polyelectrolytes. *Macromolecules* **2005**, *38*, 9304−9314.

(57) Boström, M.; Williams, D. R. M.; Ninham, B. W. The influence of ionic dispersion potentials on counterion condensation on polyelectrolytes. *J. Phys. Chem. B* **2002**, *106*, 7908−7912.

(58) Tang, Y.; Hu, X.; Cai, J.; Xi, Z.; Yang, H. An enhanced coagulation using a starch-based coagulant assisted by polysilicic acid in treating simulated and real surface water. *Chemosphere* **2020**, *259*, No. 127464.

(59) Zhang, P.; Qian, J.; An, Q.; Du, B.; Liu, X.; Zhao, Q. Influences of solution property and charge density on the self-assembly behavior of water-insoluble polyelectrolyte sulfonated poly (sulphone) sodium salts. *Langmuir* **2008**, *24*, 2110−2117.

(60) Tufenkji, N.; Elimelech, M. Correlation equation for predicting single-collector efficiency in physicochemical filtration in saturated porous media. *Environ. Sci. Technol.* **2004**, *38*, 529−536.

(61) Butt, H.-J.; Kappl, M. *Surface and Interfacial Forces*; John Wiley & Sons, 2009.

(62) Lin, M. Y.; Klein, R.; Meakin, P.; et al. Universality in colloid aggregation. *Nature* **1989**, *339*, 360−362.